Supporting information

Spatiotemporal mapping of three dimensional rotational dynamics of single ultrasmall gold nanorods

Kamalesh Chaudhari[1,2] & Thalappil Pradeep[2,*]

[1]Department of Biotechnology and [2]DST Unit of Nanoscience (DSTUNS), Department of Chemistry, Indian Institute of Technology Madras, Chennai 600 036, India. [*]Correspondence and requests for materials should be addressed to T.P. (email: pradeep@iitm.ac.in).

Table of contents

Supporting Methods

Materials and protocols in detail

Chemicals

Tetrachloroauric acid trihydrate ($HAuCl_4 \cdot 3H_2O$) (99.9%), cetyltrimethylammonium bromide (99.9%) (CTAB), sodium borohydride (99%, Fluka), (3-mercaptopropyl)trimethoxysilane (95%), trisodium citrate (>99%), glutaraldehyde (70% in H_2O), DPX mountant, poly (ethylene glycol) (average Mn 950-1,050), poly-L-lysine solution (0.1 % in H_2O) and trypsin-EDTA (0.25% in H_2O) were purchased from Sigma Chemicals. L(+) ascorbic acid (99.7%), silver nitrate (99.9%), sodium hydroxide (98%), sodium carbonate (99.8%) and ferric chloride anhydrous (98.5%) were purchased from RANKEM, India. Antibiotic (100X, Penicillin-Streptomycin-Glutamine), DMEM (Dulbecco's Modified Eagle Medium with high glucose, GlutaMAX™ Supplement and pyruvate) and FBS (Foetal Bovine Serum) were purchased from Invitrogen, USA. Details of other chemicals used are as follows, chloroform (99.5%, Thermo Fisher Scientific India Pvt. Ltd.), cystamine dihydrochloride (97%, TCI Chemicals (India) Pvt. Ltd.), bovine serum albumin (96-98%, pH 7, SRL Pvt. Ltd., India.). Apo-transferrin (Tf human recombinant) was purchased from ProSpec-Tany TechnoGene Ltd., Israel. Plastic ware for cell culture were purchased from Tarson, India. Millipore deionized water (DI) (~18.2 MΩ) was used throughout the experiments.

Synthesis of GNRs. GNRs of the dimension 30 (L) nm × 10 (D) nm were synthesized by a protocol previously reported from our group.[1] Briefly growth solution was prepared by adding 50 mL of 100 mM CTAB, 2.5 mL of 10 mM $HAuCl_4 \cdot 3H_2O$, 325 µL of 10 mM $AgNO_3$, and 350 µL of 100 mM ascorbic acid. Growth solution was incubated for five minutes and then 50 µL $NaBH_4$ (1.67 mM in ice-cold DI water) was added. After that mixture was kept undisturbed at room temperature for overnight to complete the growth of nanorods. This solution was washed using DI water after centrifugation at 7,500 rpm (20 min) once and then twice at 12,000 rpm (20 min) to remove excess CTAB. Considering that

40% of the gold retained in the form of GNRs after washing (as estimated by us), final molarity of GNR in solution (in terms of elemental gold) was ~0.2 μM. Details of these calculations are given in SI Equation 4.

Synthesis of GNPs. GNPs of the diameter 40 nm were synthesized by the Turkevich method.[2] Briefly 60 μL of 100 mM $HAuCl_4$ solution was added to 20 mL DI water and heated in a synthesizer at 400 rpm. On boiling, 240 μL of the 100 mM solution of trisodium citrate was added. After 20 minutes of continuous boiling, color of the solution changed to wine red. The solution was then cooled at room temperature. To prepare GNRaggregates, after overnight incubation of GNR_{30X10} with BSA (GNR@BSA), sample was washed to remove excess BSA (10 min, 8000 rpm) and spotted for PDFSMS.

Immobilization of GNRs on glass slide. GNRs were immobilized on a glass slide by the pinpoint immobilization method. In this method, 1 mm thick ultrasonically cleaned glass slide (SCHOTT) was flushed with 5 mL solution of (3-mercaptopropyl)trimethoxysilane (0.2 μM in chloroform). Then it was thoroughly flushed with DI water and immediately 10 μL solution of as synthesized GNR (0.02 μM) was dropped and covered with 0.145 mm thick Nexterion® Clean room cleaned glass coverslip (SCHOTT). After five minutes of incubation, coverslip was removed and glass slide was thoroughly flushed with DI water to remove loosely bound GNRs. Then 2 μL of DI water was dropped on GNR immobilized region and covered with coverslip. It was sealed with nail paint on sides to avoid drying of samples. In the overall procedure, care was taken such that only one side of slide was exposed to chemicals.

Preparation of iron loaded transferrin (holo-transferrin). For iron loading, ferric chloride solution was neutralized by sodium hydroxide (1 M) to a pH of 7. Then apo-transferrin was incubated for 1 hr with neutralized ferric chloride (molar ratio 1:2) in presence of carbonate ions followed by dialysis against DI water in 3.5 kDa molecular weight cut off Snakeskin™ Dialysis Tubing (Thermo Scientific Pierce, USA).

Conjugation of holo-transferrin to GNR surface. For conjugation of transferrin to GNR surface, amine functionalized GNRs were prepared by modifying previously reported protocol by Wang et al.[3] For this, GNRs were treated with cystamine dihydrochloride (molar ratio 1:2) with sonication for 10 mins. Then these GNRs were activated by incubation with glutaraldehyde (molar ratio 1:2) for 1 hr. Then these GNRs were washed with DI water by centrifugation at 12,000 rpm (20 min) and incubated with holo-transferrin (molar ratio 1:1) for 1 hr. Overall procedure was performed in the dark.

UV-Vis spectroscopic analysis. The samples were diluted in DI water and UV/Vis spectra were measured with a Perkin Elmer Lambda 25 instrument in the range 400-1,000 nm.

Transmission electron microscopic analysis. High-resolution transmission electron microscopy (HRTEM) of the GNR and GNR@BSA samples were carried out using a JEOL 3010 instrument at 300 kV. TEM specimens were prepared by drop casting one or two drops of aqueous solution on carbon-coated copper grids and drying in ambient.

De-pixelation of the images

For de-pixelation of the images using ImageJ software, following protocol was used.

1. Images were filtered using a Gaussian blur filter with sigma (radius) of 1.0.
2. Length and width of image was increased ten-fold in pixel units.

Contrast and brightness of the image was set to an optimum position that image should not saturate but most of the particles are visible.

Supporting Equations

Equation 1

For polar mapping, an image set collected at different angles of the analyzer was processed using the formula,

$$I_{p(x,y)} = \max\left(i_{p(x,y)}(\theta)(\theta = 0° - 360°) \right) \quad \textbf{(1)}$$

where, $I_{p(x,y)}$ is the intensity value at the pixel coordinate *(x,y)* in an image to be constructed for polar mapping and $i_{p(x,y)}$ is the scattering intensity at pixel coordinate *(x,y)* in the captured image as a function of θ. In this case, θ takes discrete values between 0^o to 360^o at the interval of 22.5^o.

Equation 2

Polar plot for each particle was determined using the following formula applied to the cropped image squares containing the particle of interest,

$$I_r(\theta) = \left(\left(i_{(m \times n)}(\theta) \right) \Big/ \max\left(i_{(m \times n)}(\theta) \right)_{(\theta = 0° - 360°)} \right) \times 100 \quad \textbf{(2)}$$

$$i_{(m \times n)}(\theta) = \left(\sum_{x=1}^{m} \sum_{y=1}^{n} I_{p(x,y)}(\theta) \right) \Big/ (m \times n)$$

where, $I_r(\theta)$ is the radial intensity in polar plot at an angle θ of the analyzer, expressed as percentage. For an image *i* captured at particular angle θ, size of the image is represented by *m* and *n*, the number of pixels in *X* and *Y* directions. $I_{p(x,y)}(\theta)$ provides the intensity at particular pixel *(x,y)* as a function of θ.

Equation 3

Polarization anisotropy was calculated using the following formula,

$$P = \frac{I_{\max} - I_{\min}}{I_{\max} + I_{\min}} \quad \textbf{(3)}$$

$\boldsymbol{I_{max}}$ and $\boldsymbol{I_{min}}$ are the maximum and minimum scattering intensities that are observed at mutually perpendicular positions of analyzer while rotation is from 0-360 degrees.

Equation 4

Molarity of GNRs in solution was calculated using the following formula,

$$M_{NP} = \frac{\left(Molarity\ \ of\ \ Au^{3+}\ \ in\ \ the\ \ solution\right) \times \left(Volume\ \ of\ \ one\ \ gold\ \ atom\right)}{\left(Volume\ \ of\ \ one\ \ GNR\right)}$$

$$M_{NP} = \frac{12MA_r}{\left(2\pi D^3 + 3\pi D^2 l\right)\rho N_A} \quad \textbf{(4)}$$

Where,

$\boldsymbol{M}$ = Molarity of Au^{3+} stock in µM

$\boldsymbol{A_r}$ = Atomic weight of Au in g

$\boldsymbol{D}$ = Diameter of GNR in cm

$\boldsymbol{l}$ = Length of GNR excluding caps in cm

$\boldsymbol{\rho}$ = Density of gold in g/cm^3

$\boldsymbol{N_A}$ = Avogadro number

Supporting Figures.

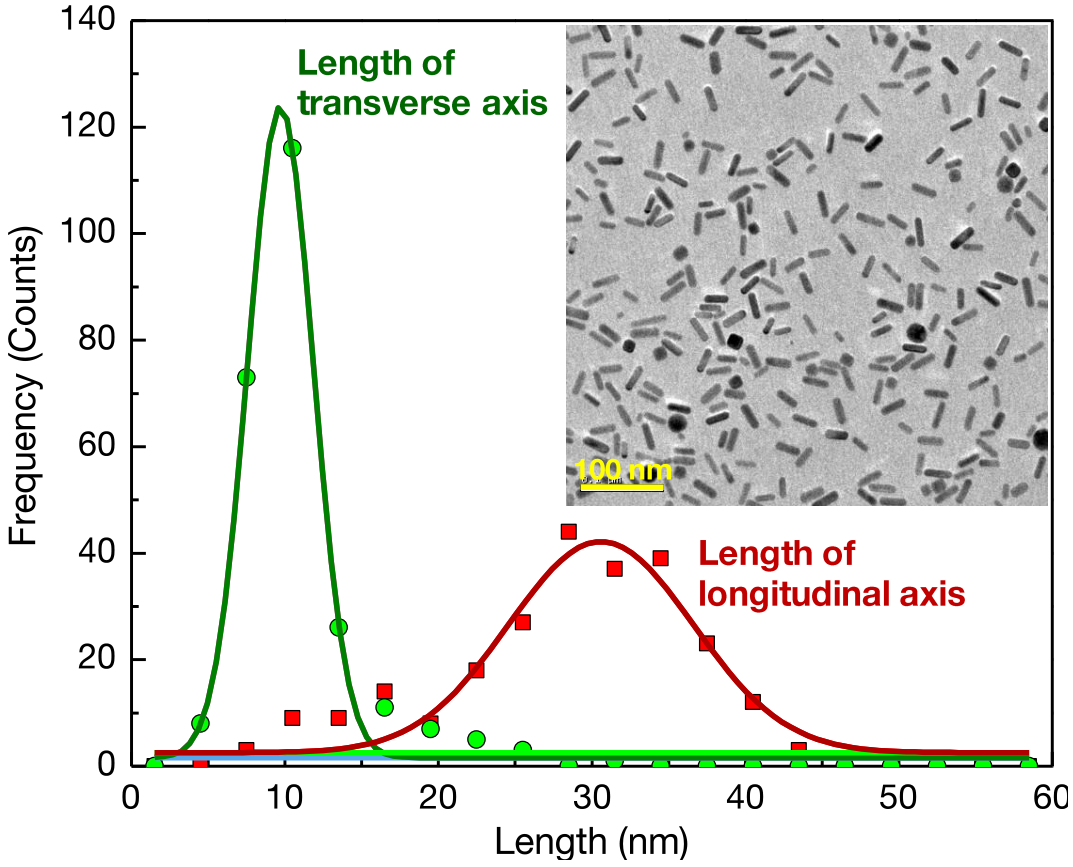

Figure S1. Size distribution of GNR_{30X10}. Histograms of the length and diameter of gold nanorods as determined from TEM show that nanorods have average length of 30 nm and diameter of 10 nm, suggesting an aspect ratio of ~3. Inset shows TEM image of the sample.

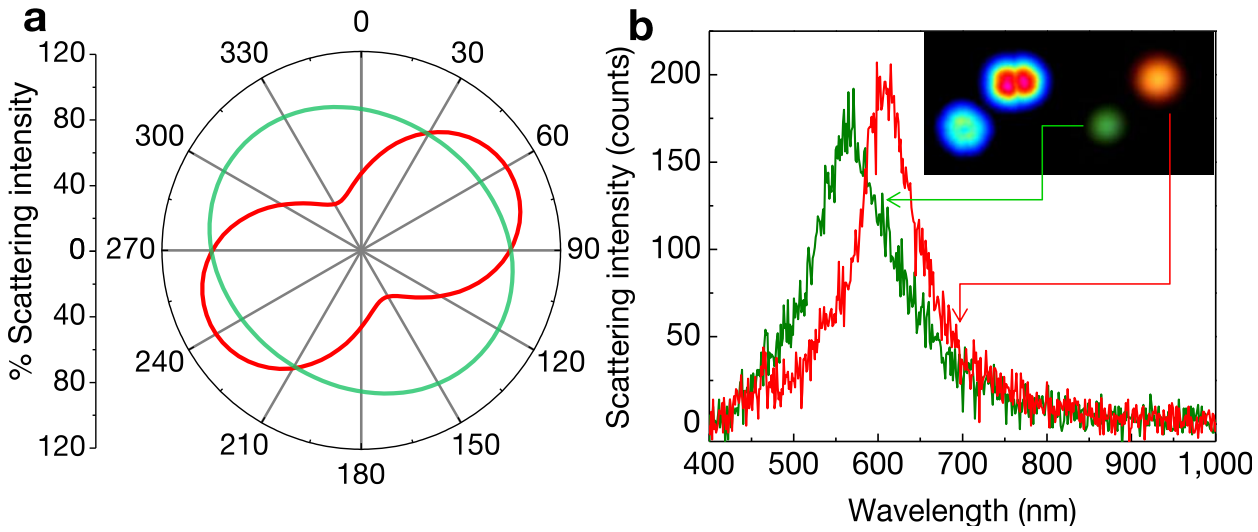

Figure S2. Polar plots and scattering spectra of a spherical gold nanoparticle (GNP) and and an anisotropic equivalent. (**a**) Polar plots of a spherical GNP (green) and an anisotropic GNP (red) for which polar maps and dark field images are shown in (**b**). (**b**) Scattering spectra suggest that they are indeed from single GNP and a single rod-shaped anisotropic GNP, respectively.

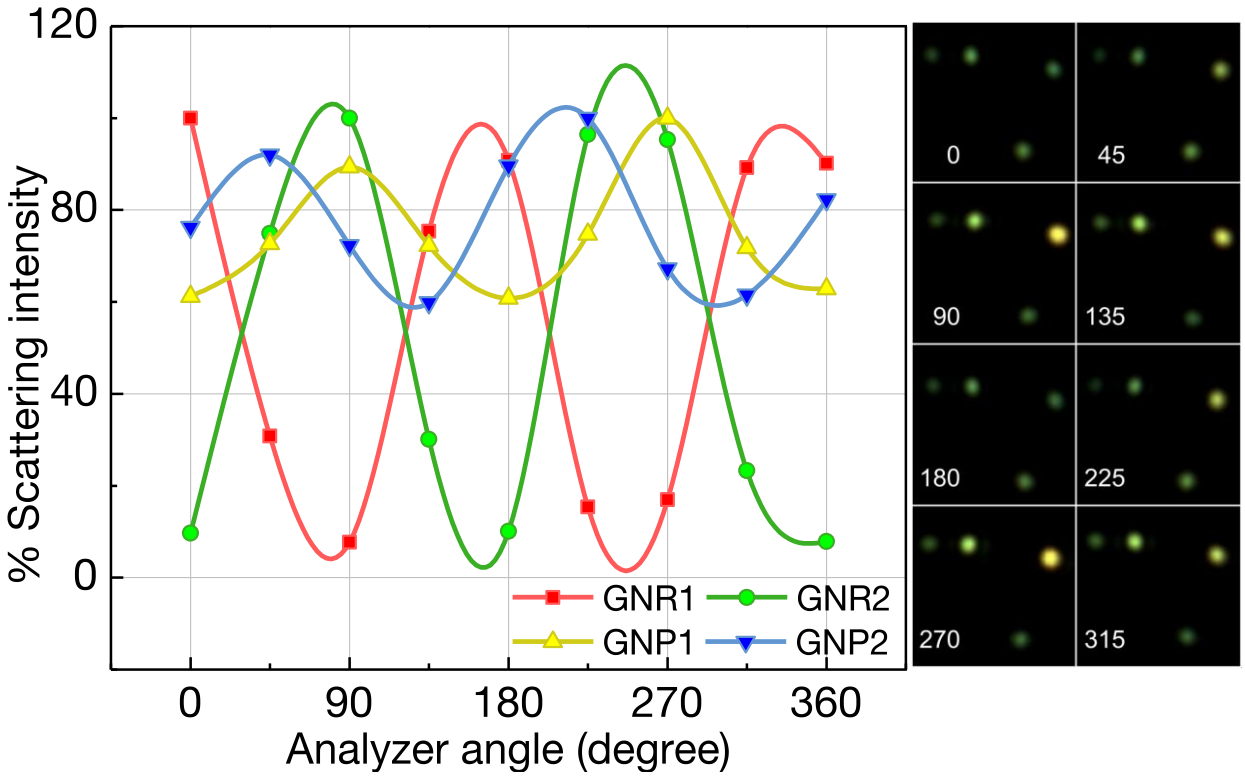

Figure S3. Anisotropy in the shape of GNPs. Graph shows percentage change in the scattering intensity of single GNPs and GNRs. It can be seen that GNPs also exhibit anisotropy depending on deviation from perfectly spherical shape. Adjacent images of GNPs are captured at different analyzer angles.

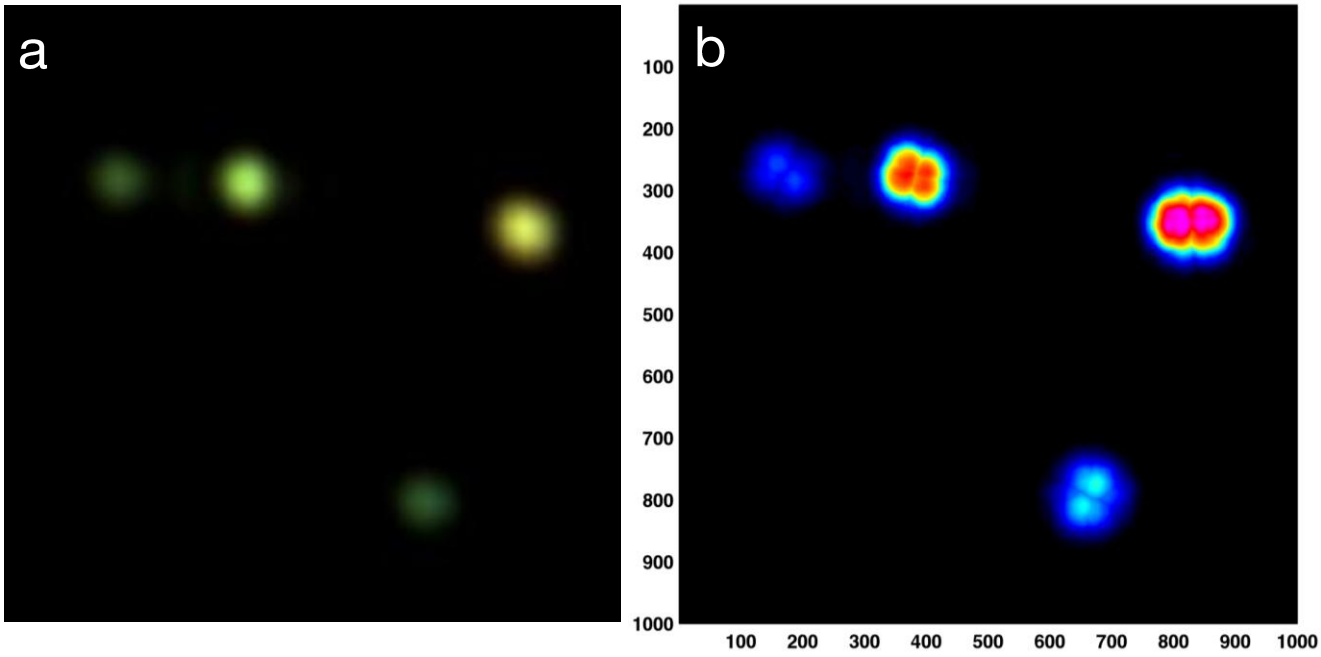

Figure S4. Polar mapping of anisotropic GNPs. (**a**) Dark field image of GNPs. (**b**) Corresponding polar maps of GNPs suggest that particles are not perfect spheres. These polar maps are determined using SI Equation 1.

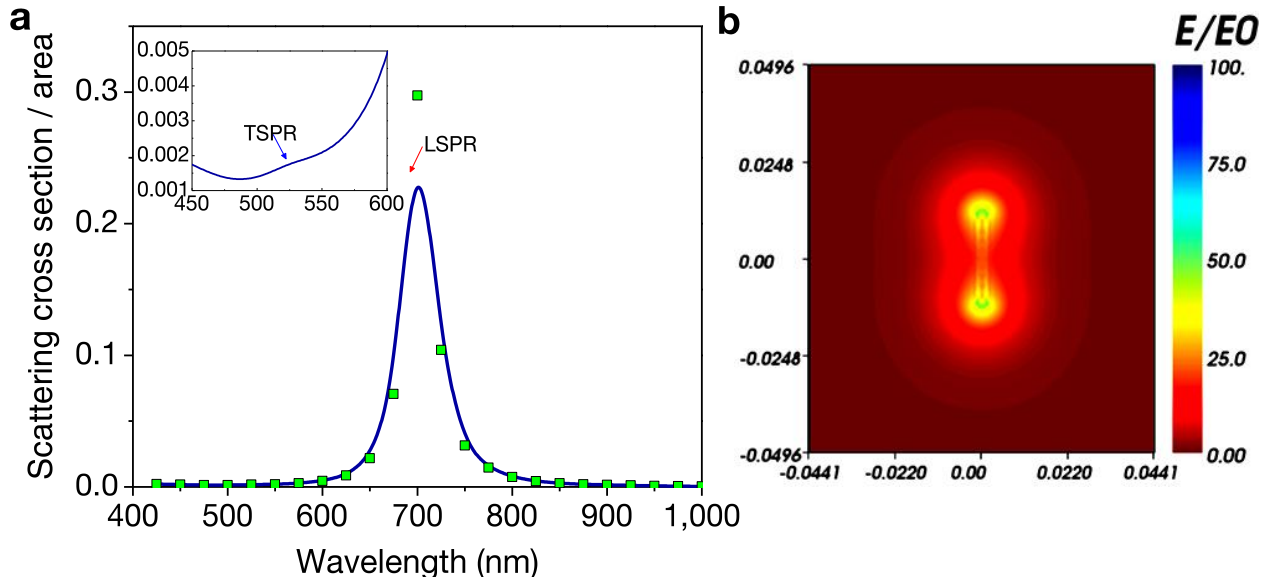

Figure S5. DDA simulations of GNR_{30X10}. (**a**) DDA simulated scattering cross section of GNR_{30X10} on unpolarized white light excitation (averaged over wavelengths 425-1000 nm and polarization of incident electric field varying from 0^{o}-360^{o}). Inset shows magnified view of the TSPR of GNR which is negligible as compared to LSPR of GNR. (**b**) DDA simulated electric near-field of GNR_{30X10} is shown where electromagnetic wave just touches the GNR. Polarization of incident electric field is along the longitudinal axis of nanorod in this simulation.

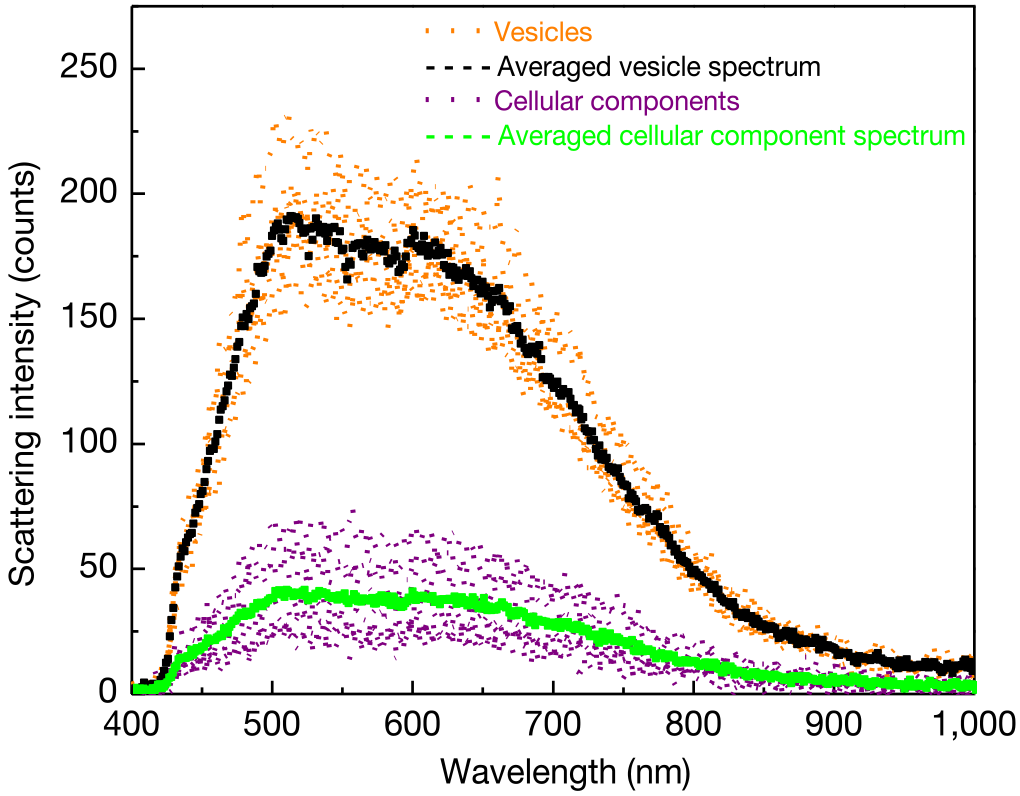

Figure S6. Scattering spectra of cellular components. It can be seen from the scattering spectra shown above that although scattering of vesicles is substantially higher than the background spectra collected from cellular components, their scattering spectra are broad with a maximum in the blue green region.

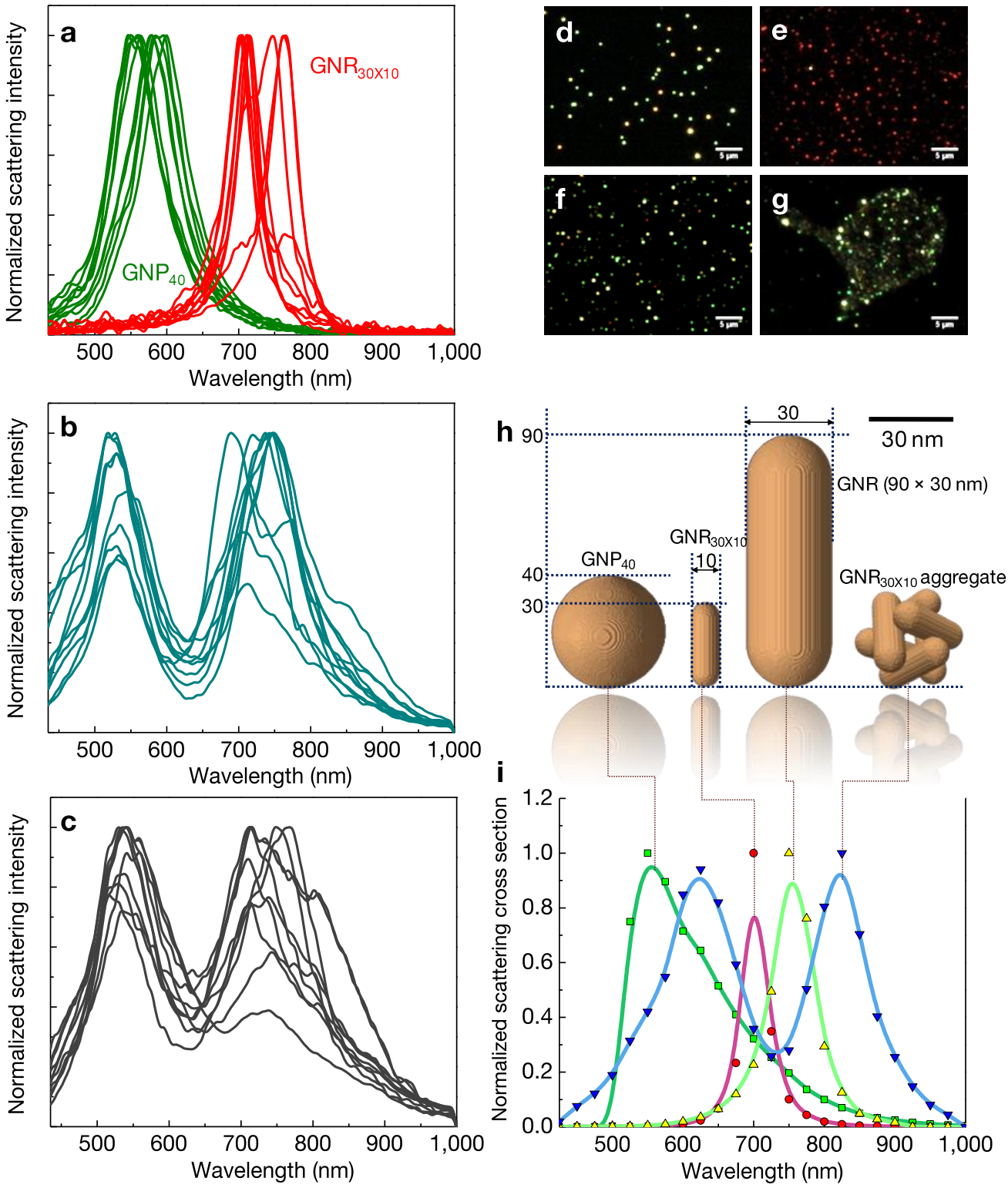

Figure S7. Examples of spectra of single GNPs, GNRs and GNR aggregates *in vitro and in vivo*. Figure shows dark field images and single particle scattering spectra of various samples collected at 100X magnification. (**a,d**) GNPs of 40 nm diameter (GNP_{40}). (**a,e**) GNRs of the dimensions 30 (L) × 10 (W) nm (GNR_{30X10}). (**b,f**) GNR_{30X10} aggregates obtained by treating it with BSA (bovine serum

albumin) protein. (**c,g**) GNR_{30X10} aggregates in HEK293 cells. Next figures are the same as the ones in the manuscript and shown here just for direct comparison. (**h**) Surface images of the model arrays generated for DDA simulations of GNP_{40}, GNR_{30X10}, GNR_{90X30} and a GNR aggregate constructed from six GNR_{30X10}. (**i**) Corresponding DDA simulated scattering cross sections of nanostructures on unpolarized white light excitation are shown here.

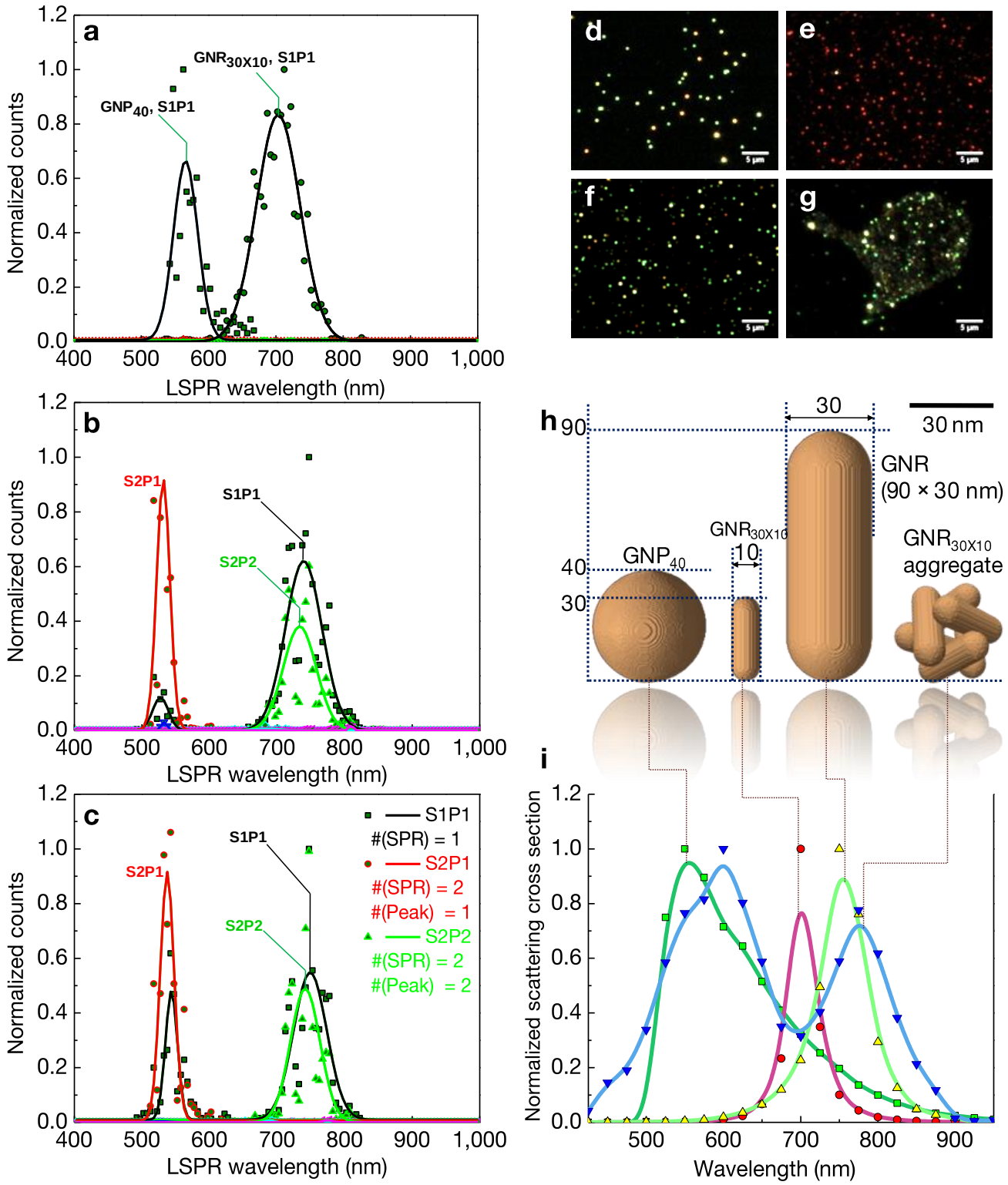

Figure S8. Gaussian curve fits to the SPR peak distributions of single GNPs, GNRs and GNR aggregates *in vitro and in vivo*. Dark field images and statistical distribution of SPR peaks determined from hyperspectral measurements of various samples at 100X magnification. (a,d) GNP40. (a,e) GNR_{30X10} (b,f) GNR_{30X10} aggregates obtained by treating it with BSA. (c,g) GNR_{30X10} aggregates in

HEK293 cells. Next figures are the same as the ones in the manuscript and shown here just for direct comparison. (h) Surface images of the model arrays generated for DDA simulations of GNP_{40}, GNR_{30X10}, GNR_{90x30} and a GNR aggregate constructed from six GNR_{30X10}. (i) Corresponding DDA simulated scattering cross sections of nanostructures on unpolarized white light excitation are shown here for comparison. Color coding for all SPR statistical distributions is provided in (c).

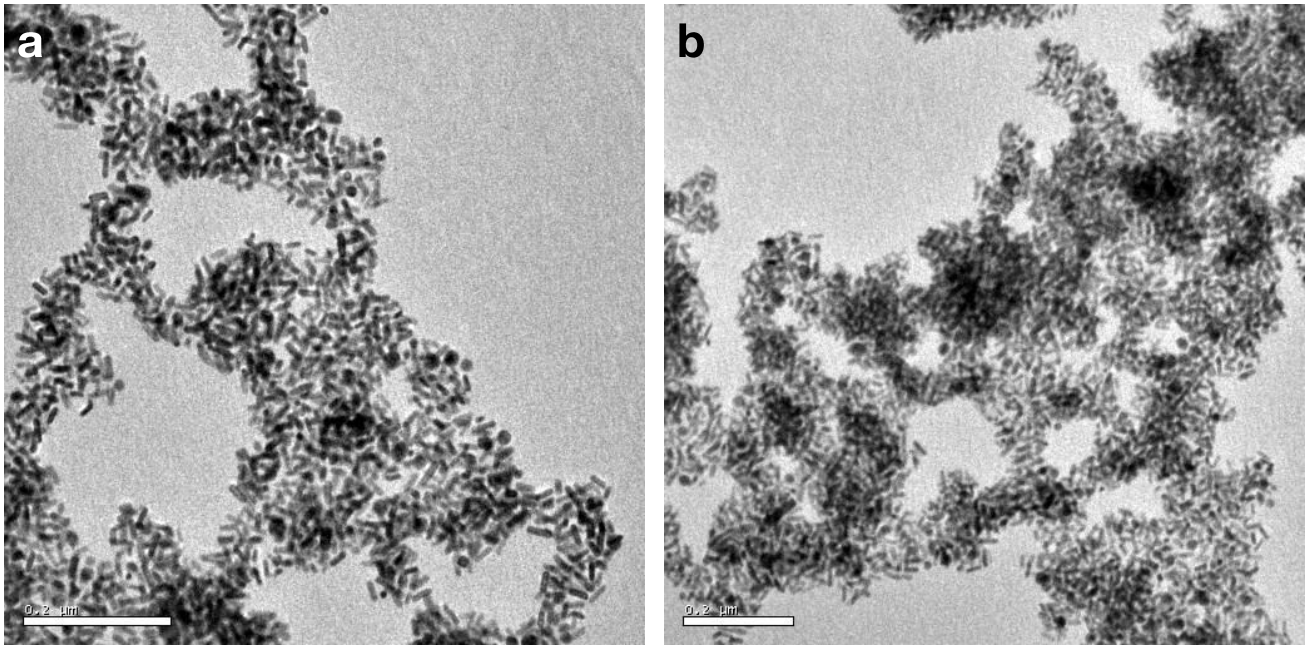

Figure S9. Aggregation of GNRs on treatment with BSA was confirmed by transmission electron microscopy (TEM). TEM images of GNR_{30X10} treated with BSA (GNR:BSA molar ratio is 1:10). Scale bar is 0.2 µm.

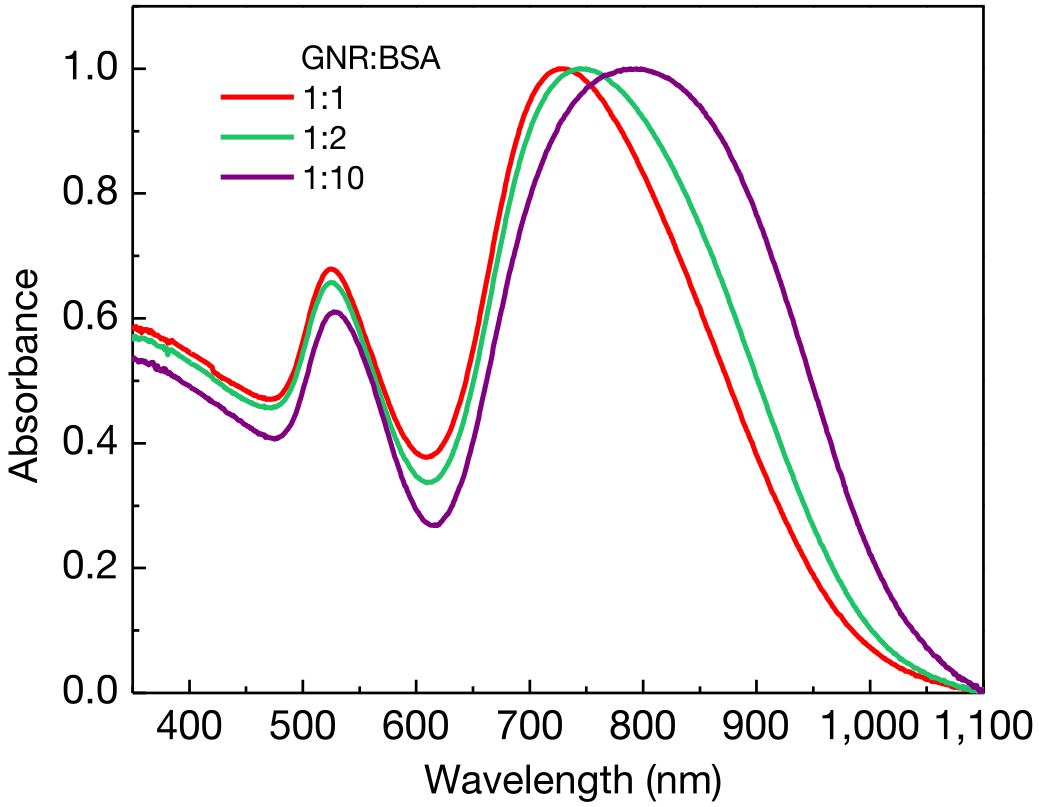

Figure S10. Aggregation of GNRs was confirmed by UV-Vis absorption. Figure shows ensemble phase UV-Vis absorption spectra of GNR_{30X10} incubated with different ratios of GNR:BSA. For uniformity in the data, 1:10 sample was used for further measurements with HSI. The spectrum of pure GNR is in Figure S11.

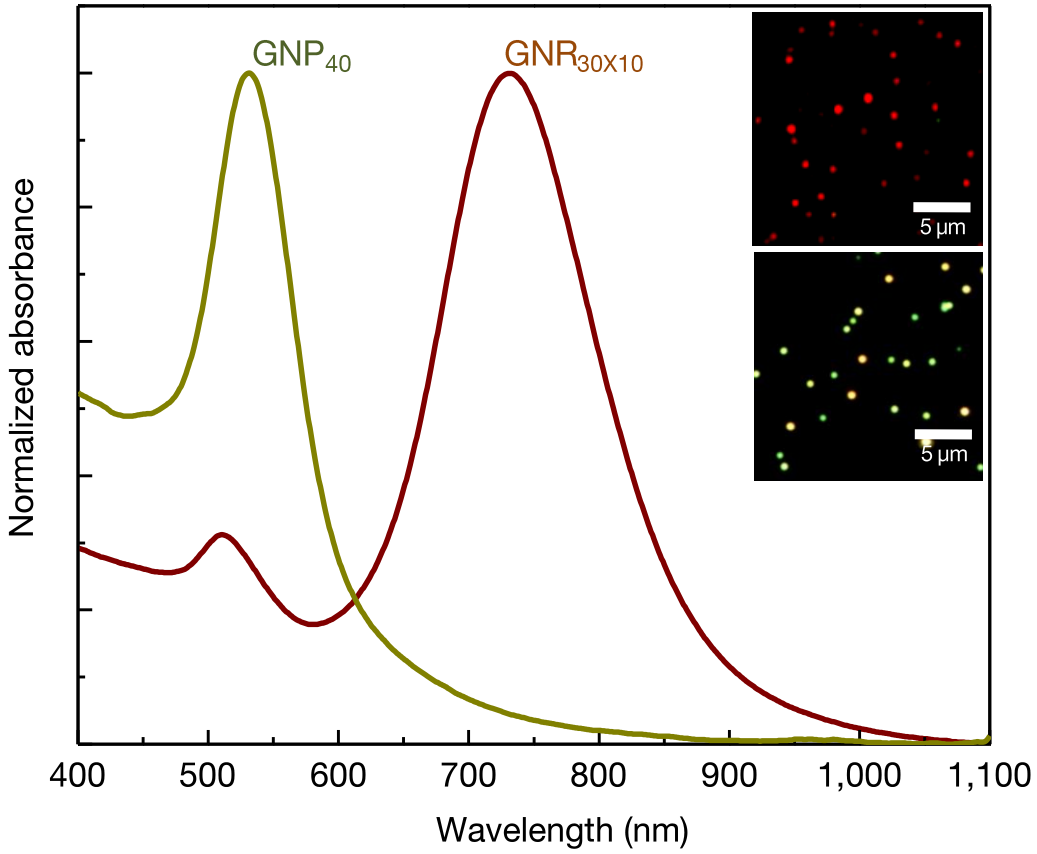

Figure S11. Ensemble phase UV-Visible spectra of GNP_{40} and GNR_{30X10}. UV-Visible absorption spectra of GNP_{40} and GNR_{30X10} solutions in deionized (DI) water. Inset shows dark field images of both these samples (red spots – GNR_{30X10} and yellowish green spots – GNP_{40}).

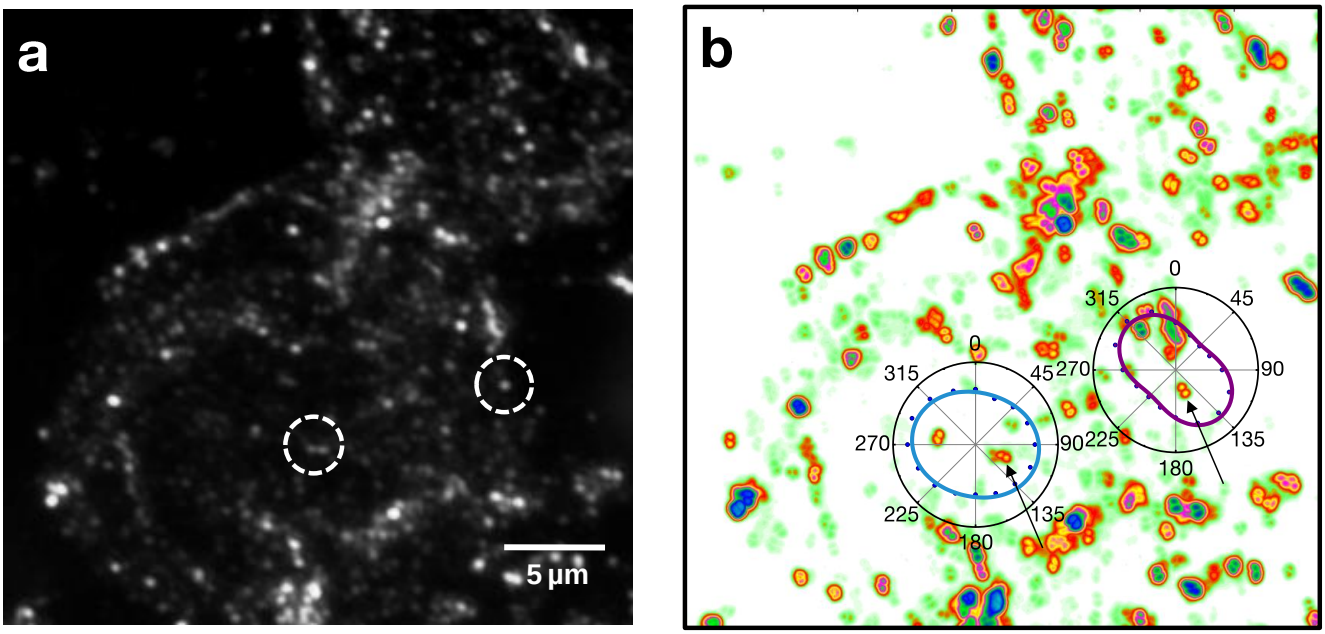

Figure S12. *In-situ* polar mapping of GNR_{30X10} in HEK293 cells. (**a**) Dark field image of HEK293 cell treated with GNR_{30X10}. Circles show nanorods for which polar plots and maps are shown in the next image. (**b**) *In-situ* polar mapping of whole cell gives an idea about polarization pattern and orientation of GNRs.

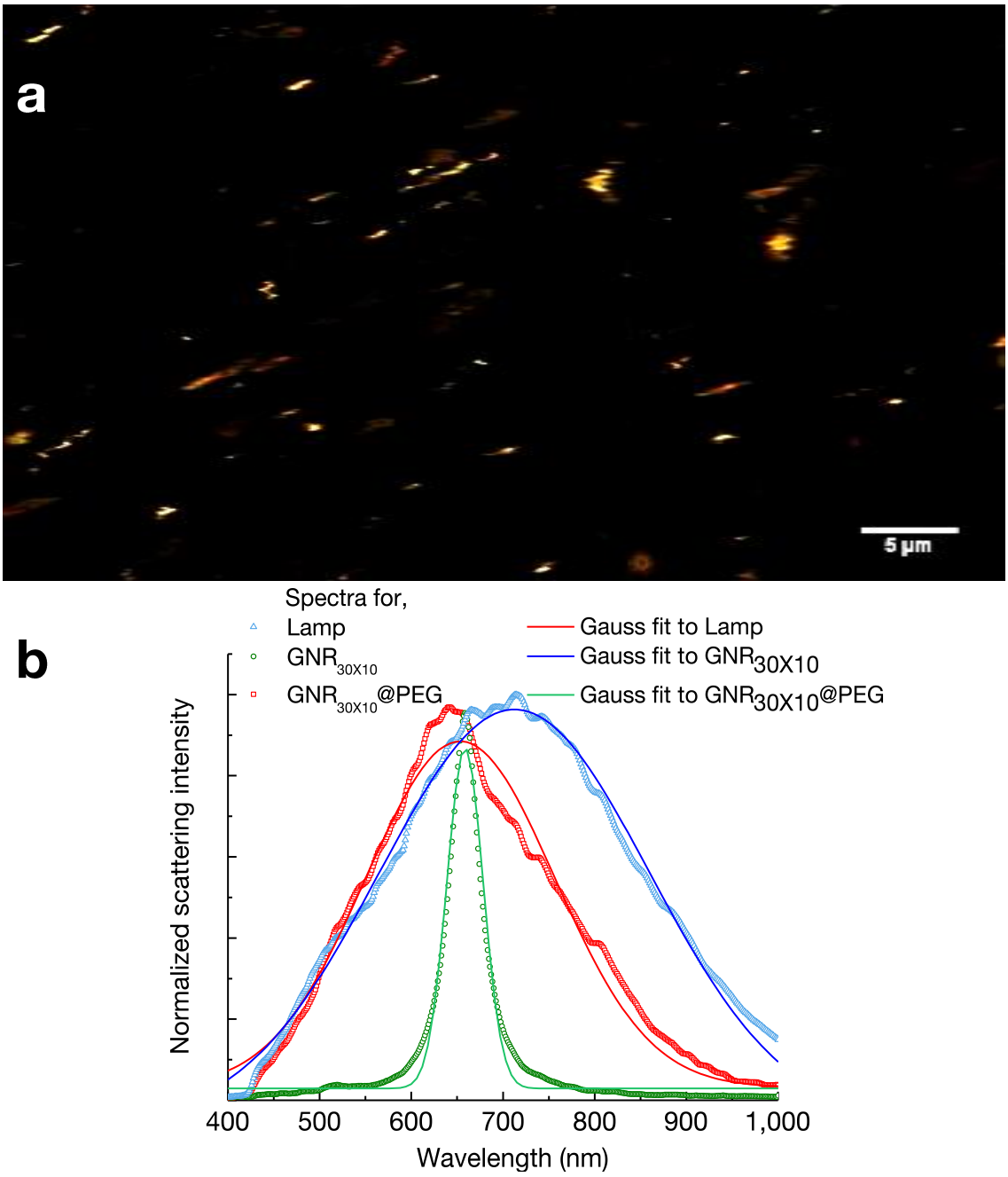

Figure S13. Scattering spectra of GNR_{30X10} in viscous PEG solution. (**a**) Hyperspectral image (HSI) of freely moving GNR_{30X10} in viscous solution of poly (ethylene glycol) (PEG). Since hyperspectral imaging is not as fast as images captured with CCD camera, during the capture of HSI, moving nanorods change their position and give a streaked appearance as shown in the above image. (**b**) Scattering spectrum of one such GNR@PEG is compared with GNR@DI (DI – deionized water) and Lamp to show that it is still single GNR and not an aggregate.

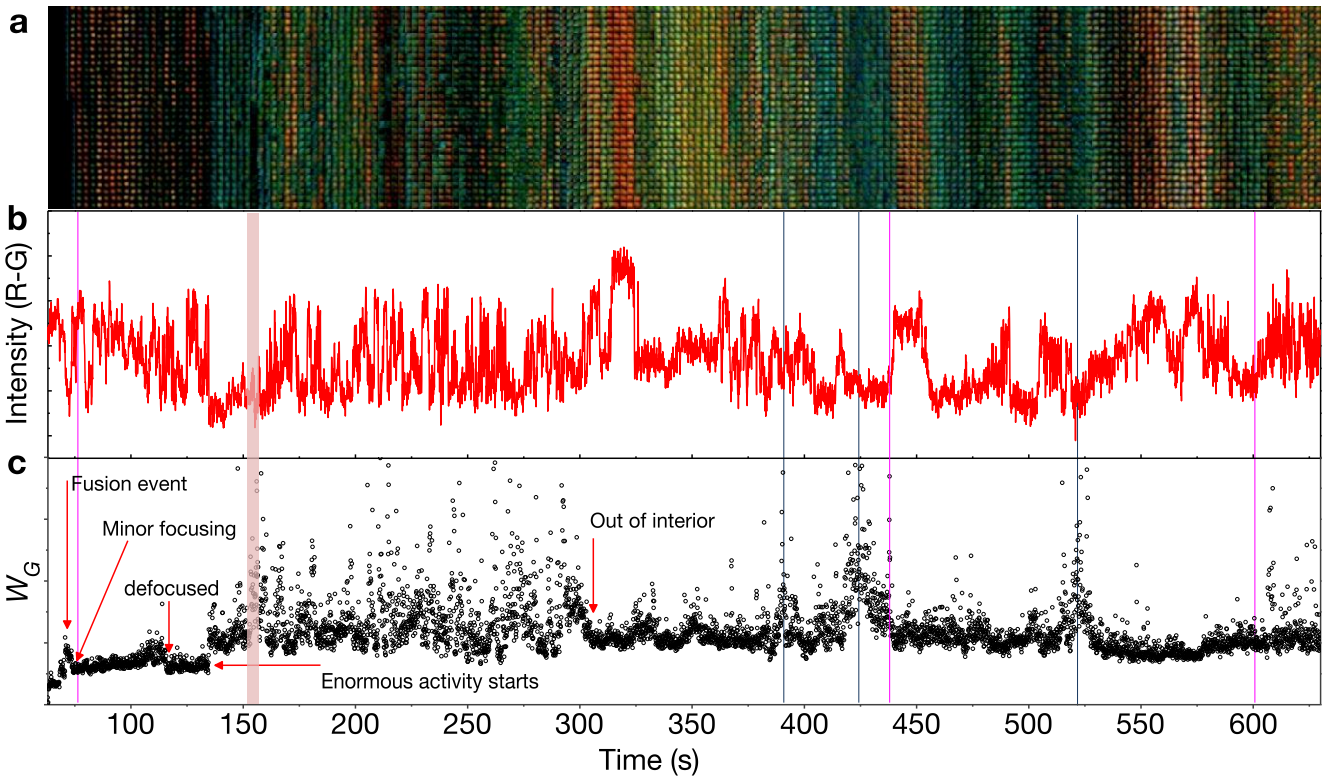

Figure S14. Color changes in GNR@Tf during its journey inside HEK293 cell. (**a**) Image shows changes in the color of GNR when images were captured through analyzer while its movement inside HEK293 cell. These 5670 images of GNR whose color and spot size changes as per the rotation and movement of GNR inside cell are extracted from real time data and stacked such that each column in the image roughly visualizes behavior of GNR in the time regime corresponding to time scale of graph in (c). Stacking is similar to the way images of GNR are stacked in Fig. 5 of the manuscript. (**b**) Temporal variations in the scattering intensity (red-green, R-G) of GNR@Tf. Time scale corresponds to the graph in (c). Pink color strips show the region where microscope focus was adjusted on particle whenever it went completely out of the focal plane. (**c**) Temporal variations in the $\boldsymbol{W_G}$ of GNR spot.

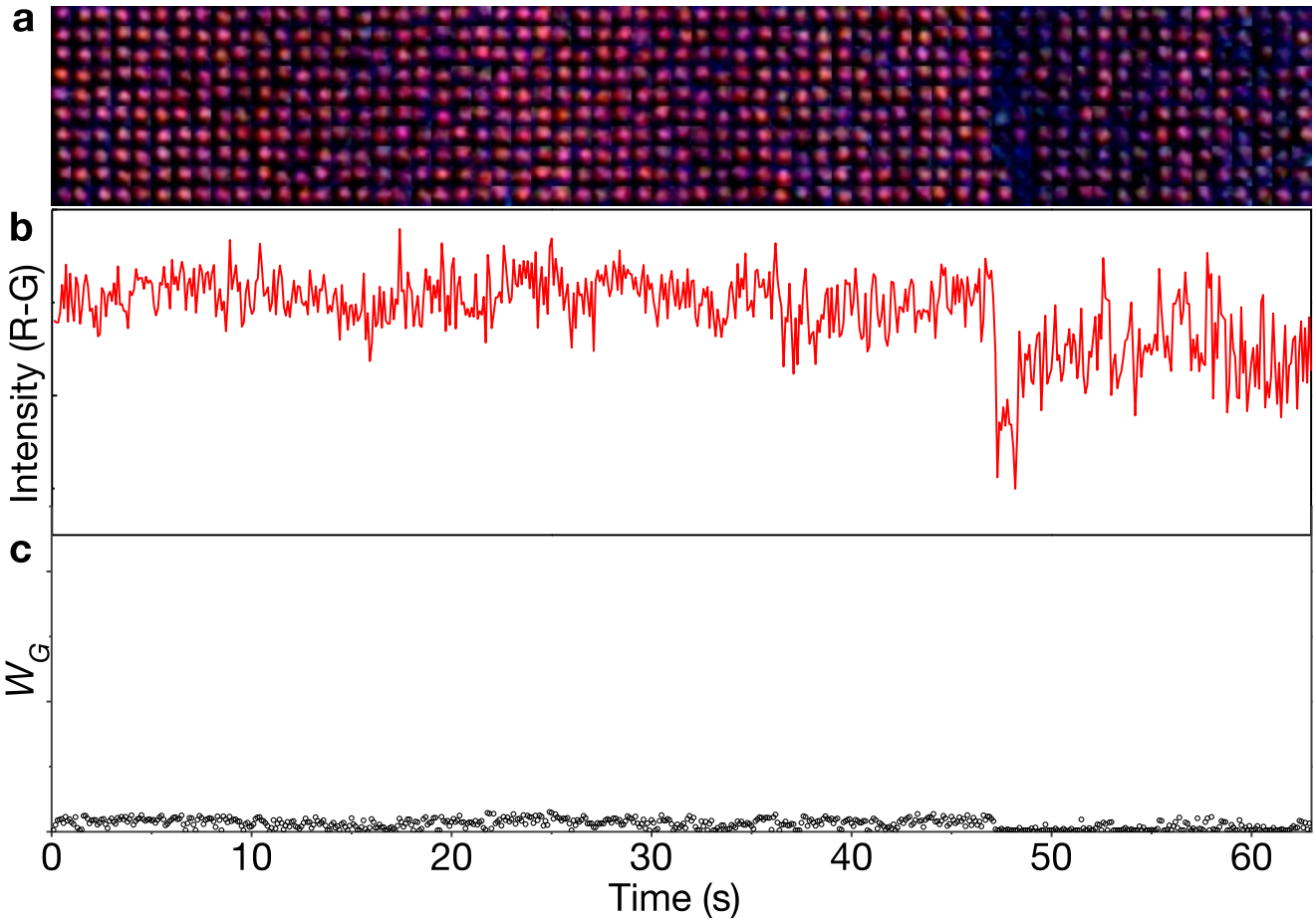

Figure S15. Behavior of GNR@Tf during initial time of intracellular observation. (**a**) Images show changes in the color of GNR when images were captured through analyzer before it starts rigorous activity inside cell. These ~630 images of GNR whose color and spot size changes as per the rotation and movement of GNR inside cell are extracted from real time data and stacked such that each column in the image roughly visualizes behavior of GNR in the time regime corresponding to time scale of graph in (c). Stacking is similar to the way images of GNR are stacked in Fig. 5 of the manuscript. (**b**) Temporal variations in the scattering intensity (R-G) of GNR@Tf. Time scale correspond to the graph shown below. (**c**) Temporal variations in the $\boldsymbol{W_G}$ of GNR spot shown at the same scale as in manuscript Fig. 6e.

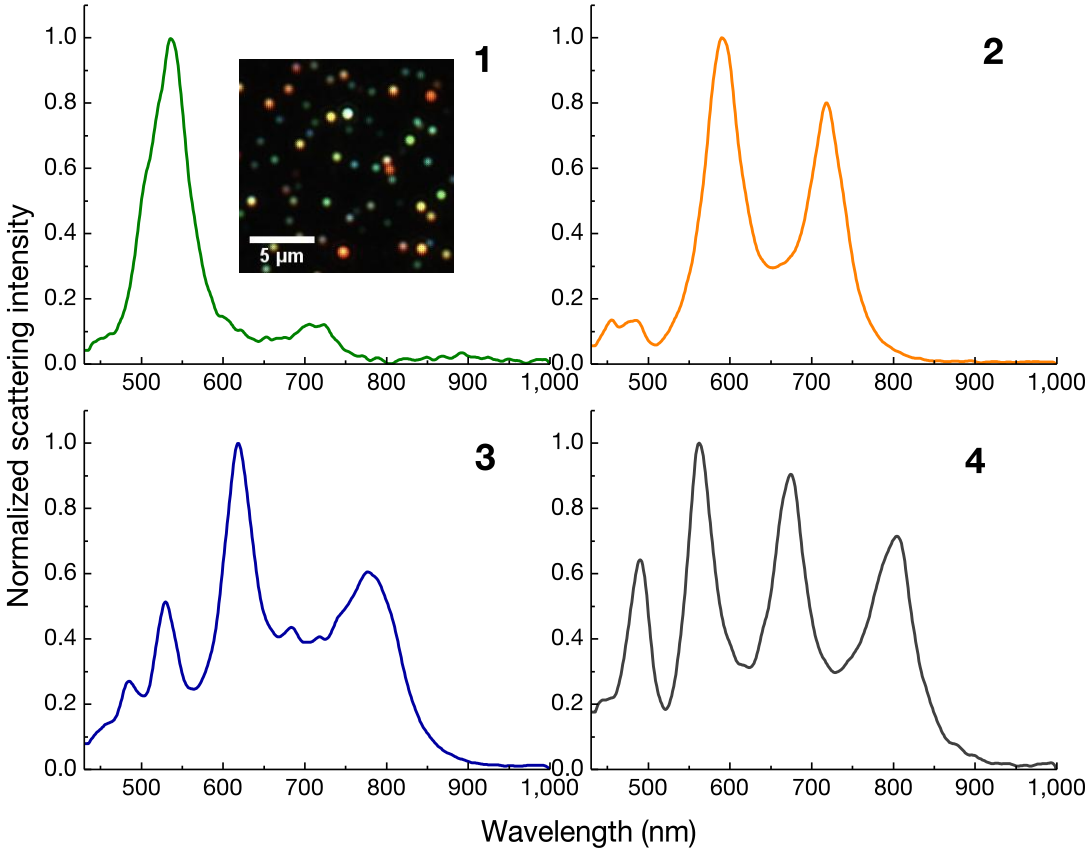

Peaks detected	Position 1	Position 2	Position 3	Position 4
1	536.0114	--	--	--
2	593.5343	717.3993	--	--
3	529.8302	618.9139	777.2375	--
4	490.6027	563.3745	674.2386	805.5502

Figure S16. Efficiency of LSPRPEAK1.001 in detecting SPR peaks. Figure shows sample spectra collected from the aggregates of citrate capped silver nanoparticles. Inset of graph 1 shows dark field image of silver nanoparticles. Hyperspectral image of the same was analyzed using LSPRPEAK1.001. Peaks detected by LSPRPEAK1.001 from the four example spectra (1-4) are shown in the table.

Supporting Discussion

Discussion 1

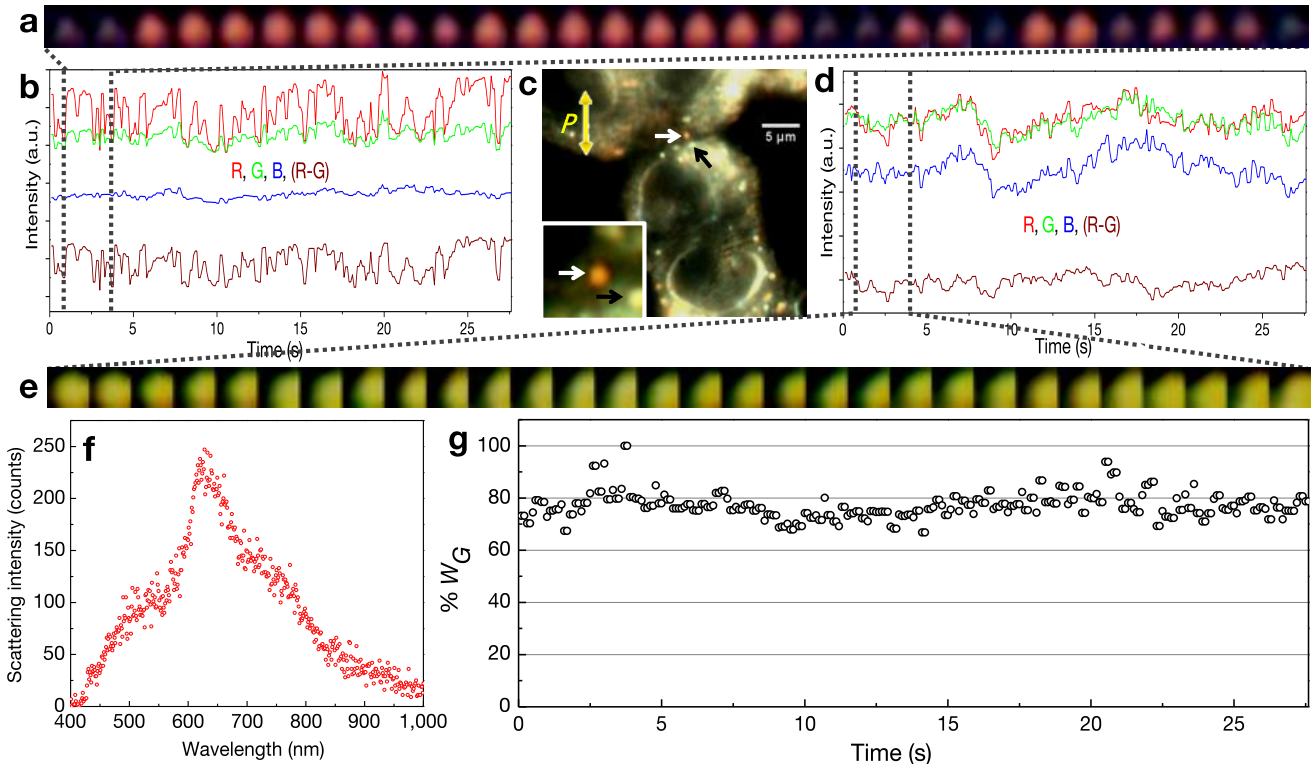

Figure S17. Real time rotational dynamics of GNR_{30X10} inside HEK293 cell. (a) Time-lapse images of a GNR_{30X10} rotating inside cell. (b) Time dependant variations in the scattering intensity (R-G) of a single rotating GNR_{30X10} in HEK293 cell. (c) Optical dark field image of live HEK293 cell with arrows indicating GNR (white arrow) and a vesicle (black arrow) under observation. Inset shows region of interest (ROI) selected for time-lapse imaging, with the particles marked. (d) Time dependant variation in the scattering intensity (R-G) of a vesicle inside HEK293 cell. (e) Time-lapse images of a vesicle. It should be noted that vesicle inside the ROI in the beginning goes slightly outside the ROI during the capture of time-lapse image sequence. See the difference between (a) and (e). (f) Scattering spectrum of a single GNR_{30X10} in HEK293 cell. Sharp LSPR peak position at ~626 nm suggests that it is indeed a single GNR and not an aggregate. (g) Temporal variations in the 2D Gaussian width (W_G) of a GNR@HEK293 spot in the image. It suggests that there is no considerable decrease or increase in the width observed and hence there was no considerable movement along the Z axis.

Real time rotational dynamics of GNR_{30X10} inside HEK293 cell. Figure S17c shows an optical dark field image of live HEK293 cell with a single GNR non-specifically entered inside HEK293 cell (GNR@HEK293). Scattering spectrum of this GNR@HEK293 shown in SI Fig. S17f confirms that it is a single GNR_{30X10}. Yellow arrow in Fig. S17c indicates the orientation of the analyzer axis which was kept constant throughout the measurement. Due to temporal variations in the scattering intensity, rotating GNR appears to be blinking inside cell. This rotating GNR with large area view of the cells is shown in Video S6 and magnified view of the same with smoothed scattering intensity variations is shown in Video S7. Figure S17b shows variations in the time (t)-dependent red, green and blue scattering intensity of GNR calculated by Equation 5,

$$I_{(C)(m\times n)}(t) = \sum_{x=1}^{m}\sum_{y=1}^{n} i_{(C)(x,y)}(t) \qquad \textbf{(5)}$$

where *C* refers to R, G or B, the isolated red, green or blue pixel images obtained after splitting the color channels of an original RGB image. Indices *m* and *n* indicate the number of pixels in the *X* and *Y* direction. $\boldsymbol{I_C}$ is the scattering intensity collected by color channel *C* at particular time *t* and $i_{(C)(x,y)}$ is the scattering intensity at pixel coordinate *(x,y)* in the captured image as a function of *t.* Since the prominent plasmonic scattering from LSPR of GNR occurs in the red region, most variations were observed in the value of $\boldsymbol{I_R}$. $\boldsymbol{I_B}$ appears to be almost inert to the changes in the orientation of GNR and $\boldsymbol{I_G}$ exhibits slight variations due to the tail of LSPR peak that lies in this region (Fig. S17b). But for the vesicle (Fig. S17d), $\boldsymbol{I_R}$, $\boldsymbol{I_G}$ and $\boldsymbol{I_B}$ follow the same trend in the variations of scattering intensity and hence confirm good S/N ratio provided by GNR_{30X10} labels. Although the vesicle inside the region of interest (ROI) goes slightly outside during the capture of time-lapse image sequence, spatial uniformity in its color justifies that scattering intensity variations can still be monitored with the available signal. Since $\boldsymbol{I_G}$ variable is close to $\boldsymbol{I_R}$ than $\boldsymbol{I_B}$ it can be used well to correct the baseline of $\boldsymbol{I_R}$ which also helps in removing the noise contributed by changes in the surrounding environment. Temporal variations in

parameter W_G (Fig. S17g) suggest that there was no considerable movement along Z axis. On the basis of these preliminary studies, we performed real time observations on the interaction of transferrin conjugated GNR (GNR@Tf) with HEK293 cells (GNR@Tf@HEK293). These observations are discussed in the manuscript.

Supporting Notes

Note 1

Description of Supporting Videos

Video S1

Three panels in this video shows, optical dark field images of a spherical GNP and an anisotropic GNP captured at different angles of the analyzer, path tracked by these particles due to displacement in the image caused by rotation of analyzer and corresponding polar maps, respectively.

Video S2

This video shows blinking of GNRs immobilized on glass substrate when their images were captured at different angles of the analyzer.

Video S3

This video shows how scattering pattern of GNRs immobilized on glass substrate changes when their images were captured at different distances from the focal plane (glass substrate), in steps of 1 μm.

Video S4

Two panels of this video show original time lapse images and images overlaid by particle tracks to indicate the fusion event between GNR and a vesicle inside the cell.

Video S5

Time lapse images of transferrin conjugated GNR moving inside HEK293 cell. A dark blue color dot is overlaid in these images to highlight the position of GNR. Other GNR appearing from the surrounding medium intermittently are indicated.

Video S6

A large area view of live HEK293 cells showing a single GNR_{30X10} (indicated by arrow) blinking due to rotation inside the cell.

Video S7

Magnified and de-pixelated view of the ROI (region of interest) showing a blinking-rotating GNR in a HEK293 cell. Corresponding variations in the scattering intensity are shown after smoothing.

References

1. Samal, A. K., Sreeprasad, T. S.& Pradeep, T. Investigation of the role of nabh4 in the chemical synthesis of gold nanorods. *J. Nanopart. Res.* **12**, 1777-1786 (2010).

2. Turkevich, J., Stevenson, P. C.& Hillier, J. The nucleation and growth processes in the synthesis of colloidal gold. *Discuss. Faraday Soc.* **11**, 55-75 (1951).

3. Wang, C.& Irudayaraj, J. Gold nanorod probes for the detection of multiple pathogens. *Small* **4**, 2204-2208 (2008).